

Rapid Imaging of Hyperpolarized Gas Using EPI

Brian Saam,^{1*} Dmitriy A. Yablonskiy,^{1,2} David S. Gierada,² and Mark S. Conradi¹

Rapid repetitive MRI of hyperpolarized (HP) gases using echo-planar imaging (EPI) has been theoretically investigated and experimentally demonstrated for ^3He in human lung. A quantitative treatment of signal attenuation and magnetization consumption for the unique circumstance of a rapidly diffusing nonrenewable magnetization source has been performed. Rapid (compared to the human respiratory cycle) and repetitive imaging of the lung gas space with EPI and a single delivered bolus of HP- ^3He is feasible using low flip angles, provided the voxels are not too small. A coarse-grid (32×64) EPI pulse sequence has been developed and implemented to image the lungs of healthy volunteers during rebreathing of a HP- $^3\text{He}/\text{N}_2$ gas mixture. A set of three 10-mm axial slices was imaged every 0.12 sec for the 36 sec duration of rebreathing, yielding a real-time visualization of ventilation. Despite some mild artifacts, the images are of good quality and show changes in gas density related to respiratory physiology. Magn Reson Med 42:507–514, 1999. © 1999 Wiley-Liss, Inc.

Key words: MRI of lung; MRI of hyperpolarized gases; EPI; rapid imaging

MRI using hyperpolarized (HP) ^3He gas is being vigorously pursued as a potentially useful imaging modality for the lung, both in humans (1–3) and in animal models (4,5). The technique is under development for the general study of pulmonary physiology and for the study of lung disease. We anticipate that HP- ^3He MRI will be useful in the study of emphysema, particularly as related to lung-volume reduction surgery (6,7).

The majority of preliminary human studies employing HP- ^3He MRI have been single-breath-hold experiments, typically employing multiple low-angle excitations and gradient-recalled echoes [e.g., FLASH (8)]. While these studies have generated spectacular static images of airways and images of ventilation on long (>10 sec) time scales, it is possible that other less expensive and technically simpler methods, including the use of inhaled inert fluorinated gases (9,10) and oxygen-enhanced MRI of lung parenchyma (11), may provide at least some of the same information.

By contrast, HP- ^3He MRI is unrivaled in its potential for depicting ventilatory *dynamics*, the inflow and outflow of gas in real time. Current methods of assessing ventilation are unable to provide information regarding *both* the movement of gas during the normal respiratory cycle and spatial localization of abnormally ventilated regions. While physiologic tests of global pulmonary function, such as

spirometry and single-breath nitrogen wash-out (12), can provide the necessary temporal resolution, there is no regionally specific information. Ventilation scintigraphy (13) can identify regions of trapped air that wash in and/or out slowly, but only on long ≈ 30 sec time scales and without cross-sectional detail. Only rapid dynamic HP- ^3He MRI has the potential to provide *both* good spatial resolution and good temporal resolution, with repetitive cross-sectional images of the lung acquired on time scales fast compared to the normal human respiratory cycle (3–5 sec).

The most important issue in determining pulse-sequence strategies for dynamic HP- ^3He MRI is the selection of a method that allows rapid and repetitive imaging of HP gas despite rapid gas diffusion and the nonrenewable nature of the magnetization. Image acquisition times must be fast compared to respiration, and efficient use must be made of the HP magnetization, which typically requires many hours to generate and is typically delivered (to human subjects) in a single bolus. Diffusion coefficients are about 10^5 larger in gases than in liquids and can cause rapid and/or differential signal attenuation and image artifacts. Consideration of the interdependence of acquisition time, signal-to-noise ratio (SNR), voxel size, and diffusive signal attenuation are not new to the MRI literature, but the unique circumstances of nonrenewable magnetization and rapid diffusion warrant a separate treatment of these effects for HP-gas MRI, particularly since the resulting implications are often radically different from those in conventional proton MRI and directly determine the optimum strategy for rapid HP-gas imaging.

Pulse sequences employing projection-reconstruction or multiple echoes are now being used to improve gas-imaging speed. Chen, Chawla, and co-workers have used projection-reconstruction to image ventilatory dynamics in the guinea pig with an effective temporal resolution of 0.1 sec (4). Ruppert, Brookeman, and Mugler have used a spiral encoding scheme to image gas-inflow dynamics in humans, whereby each view updates one sixteenth of the k -space plane every 15 msec (14). These schemes improve imaging speed and SNR and decrease diffusion artifacts by starting each acquisition at the center of k -space. However, they also require multiple radiofrequency (rf) excitations per slice resulting in a faster consumption of magnetization.

Multiple-echo sequences attempt to address both speed and the consumption of magnetization in HP-gas imaging. It is well understood from NMR that the transverse magnetization produced by a resonant rf excitation may be repeatedly rephased by gradient reversals to produce multiple gradient echoes for a time $\sim T_2^*$. Although this property has been exploited in conventional proton MRI, it is particularly attractive in HP-gas MRI, since any transverse magnetization remaining after the acquisition of a single echo (as with FLASH, for example) is unused and permanently lost. Echo-planar imaging (EPI) (15) was the first and

¹Department of Physics, Washington University, St. Louis, Missouri.

²Mallinckrodt Institute of Radiology, Washington University, St. Louis, Missouri. Preliminary results presented at the ISMRM, 6th Annual Meeting, Sydney, Australia, 1998.

Grant sponsors: Washington University Department of Radiology; Mallinckrodt Medical, Inc.

*Correspondence to: Brian Saam, Department of Physics, CB 1105, Washington University, St. Louis, MO 63130-4899.

Received 29 September 1998; revised 24 March 1999; accepted 7 May 1999.

© 1999 Wiley-Liss, Inc.

simplest of the multiple gradient-echo sequences. A preliminary report (16) of the use of EPI for rapid ^3He MRI in human lung has been made. Segmented EPI has been used to decrease acquisition times in HP- ^3He static breathhold studies (17). HP- ^{129}Xe phantoms have been imaged (18) using sequences such as EPI, RARE (19), and GRASE (20). The latter two sequences employ periodic 180° rf pulses and may thus prove more technically difficult to implement for HP gases than EPI: In addition to their intended effect on the transverse magnetization, 180° pulses also reverse the entire supply of remaining longitudinal magnetization, leading to permanent magnetization losses for inversions that are not perfect and homogeneous. We have thus chosen EPI (complete raster-like scan of two-dimensional (2-D) k-space with a single rf excitation) as a representative sequence in both theoretical and experimental work on the use of multi-echo sequences in dynamic HP-gas MRI.

We demonstrate here that EPI can give extremely short image acquisition times with the least consumption of the nonrenewable ^3He magnetization, fulfilling the requirements for dynamic HP- ^3He MRI by enabling many images to be acquired rapidly from the same bolus of HP gas. We further show that these benefits can be realized despite the rapid diffusion of helium gas in the lung as long as the voxel size is not too small. The arguments we present can be generalized to any rapid imaging sequence. Finally, we present HP- ^3He images of lung ventilation in healthy volunteers acquired using our coarse-grid EPI technique.

RAPID GAS IMAGING

Rapid multi-echo sequences are particularly suited to the use of a nonrenewable hyperpolarized magnetization source. In conventional multi-echo MRI, a trade-off exists between imaging speed and the desire to compensate increased noise (from increased bandwidth) with greater signal intensity; additional signal intensity can always be obtained by averaging, after waiting for some time $\sim T_1$. In HP-gas MRI, there is no T_1 recovery, and any unused transverse magnetization is permanently lost. Image acquisition time is limited only by bandwidth and gradient slew rates, but the magnetization must be rationed throughout the image acquisition, and T_1 decay continuously destroys any unused longitudinal magnetization.

Signal-to-Noise Considerations

If we take the ^3He lung MR images obtained with FLASH by several groups in recent years (21,22) as a SNR standard, we can compare EPI to FLASH in order to illustrate the power of the multi-echo sequence for HP-gas MRI. The FLASH images were typically acquired with 5° – 10° tip angles, so that the small tip-angle limit ($\sin \theta \approx \theta$) is appropriate. We also assume both sequences are chosen for optimum use of the transverse magnetization, using equal data acquisition periods of order $T/2$ after each rf excitation. That is, the n EPI phase-encoding steps comprising a 2-D slice fit into the time of one FLASH phase-encoding step. In our analysis, we neglect differences between the two sequences in the times required for the rf pulse(s), slice-

selection, and phase-encoding gradients, as these result only in small numerical corrections to our comparison. To compensate the increased noise due to the n times larger EPI bandwidth, the tip angle for EPI (still assumed small) is increased by \sqrt{n} . Since the magnetization remaining after a pulse of small tip angle θ is $M_0 \cos \theta \approx M_0(1 - \theta^2/2)$, the magnetization loss after forming one image is the same for both sequences, with the n small pulses of FLASH consuming the same amount as the larger single EPI pulse (see Table 1). Under these conditions, EPI obtains the same image with the same SNR and consumption of magnetization as FLASH, but n times faster. This analysis may be reworked to produce a direct comparison of the SNR or magnetization consumption as well as imaging rate, but the EPI approach will always be advantageous. For example, one could imagine a FLASH sequence able to generate n phase encoding steps as fast as EPI. Using the same tip angle, the two sequences would then have the same SNR and imaging rate, but EPI would consume n times less magnetization.

The repetitive imaging of gases may be accomplished through careful choice of voxel size, which can dramatically increase the number of sequential EPI images that may be acquired from a single HP-gas bolus. For voxels of volume ΔV and some initial magnetization M_0 , the signal-to-noise ratio in each voxel is

$$\text{SNR} \propto M_0 \Delta V \theta \sqrt{n\tau}. \quad [1]$$

Here $M_0(\Delta V)$ is the total longitudinal magnetic moment in a single voxel. A fraction θ of this moment (recall $\sin \theta \approx \theta$ here) is made transverse to generate a signal. τ is the read-out time required for each of n phase-encoding steps; $(n\tau)^{-1/2}$ is the square root of the effective bandwidth determining the noise in each voxel. The consumption of magnetization per image ΔM is $M_0\theta^2/2$, allowing N such images to be acquired, where $N \approx M_0/\Delta M = 2/\theta^2$. Here we do not attend to details such as whether the pulse angle is incremented to deliver a linear consumption of M versus time (23,24), neglecting the small change in ΔM from pulse

Table 1
A Comparison of Imaging Parameters for EPI and FLASH Sequences for Rapid Repetitive Imaging Using a Nonrenewable Magnetization Source and a Low Flip Angle ($\sin \theta \approx \theta$)^{*}

| Parameter | FLASH | EPI |
|------------------------------------|----------------------|----------------------|
| Tip angle (chosen) | θ | $\sqrt{n}\theta$ |
| rf excitations | n | 1 |
| Energy deposition proportional to: | $n\theta^2$ | $n\theta^2$ |
| Acquisition time | nT | T |
| Magnetization consumed | $M_0 n \theta^2 / 2$ | $M_0 n \theta^2 / 2$ |
| Signal proportional to: | θ | $\sqrt{n}\theta$ |
| Noise proportional to: | $1/\sqrt{nT}$ | $1/\sqrt{T}$ |
| SNR proportional to: | $\theta\sqrt{nT}$ | $\theta\sqrt{nT}$ |

^{*}The values in each column correspond to the acquisition of one slice requiring n phase-encoding steps, where M_0 is the initial longitudinal magnetization. The acquisition time T for each FLASH phase-encoding step is equal to the acquisition time for all n EPI phase-encoding steps. In either case, T is chosen to be approximately equal to $T/2$.

to pulse. Thus in terms of the number of available images N ,

$$\text{SNR} \propto M_0 \Delta V \sqrt{2\pi r/N}. \quad [2]$$

Thus, an increase in linear voxel dimensions provides a corresponding *sixth-power* increase in the number of images N that can be acquired at constant SNR. For example, by doubling the linear dimensions of the voxel, the same SNR can be obtained with θ reduced by a factor of 8, reducing the amount of magnetization destroyed by a factor of 64, allowing 64 times as many images to be obtained from a single bolus of HP- ^3He magnetization. We again emphasize that these results are unique to the use of a nonrenewable magnetization source.

Transverse Decay

In order for EPI to take advantage of the transverse coherence remaining after each echo, the transverse decay rate must be slow. The transverse relaxation of ^3He in the magnetically inhomogeneous lung may be characterized according to the classification introduced by Yablonskiy (25), which defines three distance scales (microscopic, macroscopic, and mesoscopic) according to the distance over which the field changes compared to voxel size. Macroscopic field inhomogeneities extend over lengths much larger than the voxel size and can be partially corrected with proper shimming of the applied field. Microscopic inhomogeneities result in the intrinsic T_2 relaxation. For a gas in the fast-collision limit, $T_2 = T_1$, for ^3He , $T_1 \approx 30\text{--}40$ sec in the lung (26) and is presumably determined by wall relaxation and interaction with oxygen (27). Therefore, T_2 relaxation is negligible. Mesoscopic inhomogeneities are tissue specific and cause spin dephasing inside each voxel, arising from local susceptibility variations. These appear to be smaller for ^3He gas than for protons in lung tissue, where T_2^* is only a few milliseconds (28). We have conducted preliminary experiments indicating that the intravoxel T_2^* is approximately 20 msec for ^3He in human lung in a field of 1.5 T. The larger T_2^* for the gas is likely due to some combination of the gas being farther from the tissue interface, the nearly spherical shape of the alveoli, and motional averaging of the inhomogeneities by diffusion of the gas. Similar times for lung T_2^* have been measured in guinea pigs (29). If susceptibility-gradient effects are dominant, we can reasonably conclude that EPI is at least viable if the acquisition time is kept below 20 msec. For example, an entire axial slice, consisting of 32 gradient echoes (phase-encoding steps) at 0.6 msec/echo (appropriate to our scanner hardware), could be acquired with a single rf excitation and 5 mm resolution in a typical human lung.

A fourth source of transverse decay, diffusion through the imaging gradients, must also be treated for the case of rapidly diffusing gas. This decay is an exponential function of the diffusion coefficient D and the square of the imaging gradient. For gas imaging, D is typically 10^5 times larger than for liquids, which affects a much broader range of physiologically relevant voxel sizes. Indeed, since EPI

gradients are particularly strong, these facts led us and perhaps others to dismiss or at least defer consideration of multi-echo techniques for HP-gas MRI. However, with a carefully chosen voxel size, the attenuation is tolerable, and the above described benefits in imaging speed and efficient use of hyperpolarized magnetization can still be realized. In conventional MRI, echo attenuation in a multi-echo sequence is normally dominated by T_2 and (in lung tissue, for example) bulk susceptibility effects. For gas imaging, it is instructive to derive an expression for echo attenuation versus time due to diffusion through imaging gradients. We start with the Torrey modification (30) to the Bloch equations for transverse magnetization M_+ (\mathbf{r} , t) = $M_x + iM_y$ in the rotating frame:

$$\frac{\partial M_+}{\partial t} = i\gamma \mathbf{G} \cdot \mathbf{r} M_+ - D\nabla^2 M_+, \quad [3]$$

where D is the diffusion coefficient (assumed isotropic) and \mathbf{G} is the imaging gradient, which we assume to be dependent on time but spatially invariant over the sample. We have neglected T_2 effects. The temporal and spatial variables in Eq. [3] are separable and the solution is $M_+ = M_+^{(x)} M_+^{(y)} M_+^{(z)}$, where (31)

$$M_+^{(x)}(x, t) = A_x(t) \exp\left[-ix \int_0^t \gamma G_x(t') dt'\right]. \quad [4]$$

The position-independent fractional amplitude of M_+ remaining at time t is

$$A_x(t) = A_0 \exp\left\{-D\gamma^2 \int_0^t \left[\int_0^{t'} G_x(t'') dt''\right]^2 dt'\right\}, \quad [5]$$

with A_0 representing the initial transverse magnetization. Similar expressions hold for the y - and z -component solutions.

We now consider the acquisition of a 2-D slice with EPI (see Fig. 1). If τ is the duration of the readout window for each phase-encoding step, then the loss of magnetization due to diffusion in the frequency-encoding (x) direction given by Eq. [5] occurs independently for each interval τ between the echo peaks (32). Here we assume no time delay between successive acquisition windows. Solving

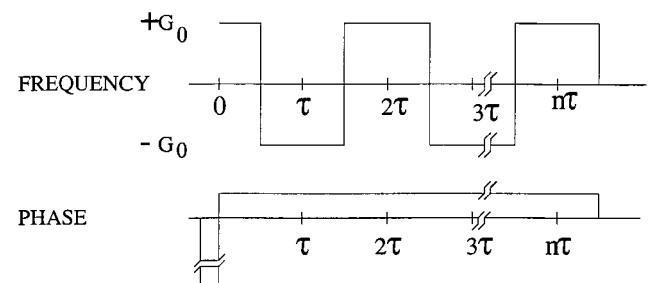


FIG. 1. The EPI frequency-encoding (read-out) and phase-encoding gradients used to consider the effects of diffusion through imaging gradients on signal amplitude. For a more practical sinusoidal readout gradient, the peak amplitude corresponding to the identical linear voxel dimension Δx would be $\pi G_0/2$.

Eq. [5] for a square-wave gradient of peak amplitude G_0 , we obtain

$$\frac{A_x(\tau)}{A_0} = \exp\left(\frac{-D\gamma^2 G_0^2 \tau^3}{12}\right). \quad [6]$$

The amplitude of the n th echo at $t_n = n\tau$ is given by raising the exponential in Eq. [6] to the n th power:

$$\frac{A_x(t_n)}{A_0} = \exp\left(\frac{-D\gamma^2 G_0^2 \tau^3 t_n}{12}\right). \quad [7]$$

Using the resolution criterion $\gamma G_0 \tau \Delta x = 2\pi$, where Δx is the linear voxel dimension in the read-out direction, we arrive at

$$\frac{A_x(t_n)}{A_0} = \exp\left(\frac{\pi^2}{6} \frac{t_n}{T_D}\right). \quad [8]$$

Here $T_D = (\Delta x)^2/2D$ is the diffusion time across a voxel in the x direction. It can be shown that the square-wave readout gradient gives the least echo attenuation for a given resolution Δx and that for the practical case of a sinusoidal gradient, the exponential co-factor in Eq. [8] is $\pi^2/4$ instead of $\pi^2/6$.

For the phase-encode direction, there are two intervals of equivalent attenuation, one on each side of $k_y = 0$ (the central echo). The initial intense but short negative wind-up gradient causes negligible diffusive attenuation compared to the constant weaker gradient that follows it (see Fig. 1). This follows directly from the fact that the limit of the argument of the exponential in Eq. [5], taken as $t \rightarrow 0$ while holding Δx (i.e., the integral over dt') constant, is zero. If we assume that n echoes cover the entire slice, then the phase-encoding gradient amplitude is n times smaller than the read-out gradient (per unit voxel dimension) and the interval of diffusive attenuation is n times longer. Using Eq. [6] with $\tau \rightarrow n\tau$ and $G_0 \rightarrow G_0/n$, we find for $A_y(t_n)$ an expression identical to that for $A_x(t_n)$ in Eq. [8], bearing in mind that G_0 and T_D will have different values for $\Delta y \neq \Delta x$ and/or anisotropic diffusion. We note that this expression is strictly valid for only three points: $t = 0$, the central echo at $t = TE$ ($k_y = 0$), and the last echo at $t = t_n$. The intervening shape is a t^3 -exponential with a decreasing second derivative for $k_y < 0$ and an increasing second derivative for $k_y > 0$. Similar behavior occurs for $A_x(t)$ between each echo. Nevertheless, for simplicity we express the total attenuation $A(t)$ in the 2-D EPI experiment with a sinusoidal readout gradient and $\Delta y = \Delta x$ as

$$\frac{A(t)}{A_0} = \frac{A_x(t)A_y(t)}{A_0} = \exp\left(-\frac{5\pi^2}{12} \frac{t}{T_D}\right). \quad [9]$$

For a square-wave read-out gradient, the exponential co-factor in Eq. [9] is $\pi^2/3$.

Figure 2 presents $A(t)$ versus t in Eq. [9] for several values of the resolution Δx (with $\Delta y = \Delta x$) in the range of 1–10 mm for $D = 0.25 \text{ cm}^2/\text{sec}$. We assume an entire slice is acquired with a single rf excitation using a 600 μsec read-out window and $400 \times 400 \text{ mm}$ field-of-view (FOV). The

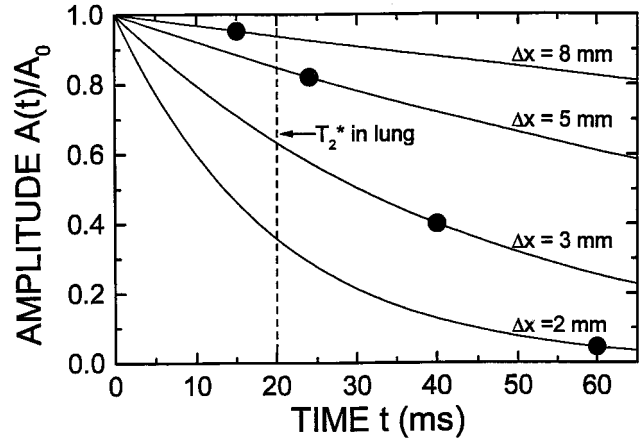


FIG. 2. EPI signal attenuation as a function of time for several values of linear voxel dimension Δx (square voxels assumed). The curves correspond to a sinusoidal readout gradient (Eq. [9]) and a diffusion coefficient $D = 0.25 \text{ cm}^2/\text{sec}$ for ^3He , appropriate for the human lung. The dashed line indicates the T_2^* from bulk susceptibility for the lung at 1.5 T. The dots indicate TE (central echo at $k_y = 0$) for each value of Δx for a 600 μsec read-out gradient and 400 mm FOV.

read-out and FOV parameters are typical for EPI and human lung and were similar to those used to obtain the images presented below. The value of D is based on our own preliminary measurements and those of Mugler, Brookeman, and co-workers (33), both of which determine the range of apparent diffusion coefficients (ADCs) for ^3He to be 0.2–0.3 cm^2/sec , smaller than the free-air value ($D \approx 1 \text{ cm}^2/\text{sec}$) due to restricted diffusion in the alveoli. As voxel size decreases, the magnitude of the exponential argument in Eq. [9] grows rapidly not only because T_D is smaller, but also because TE (indicated for each value of Δx by the black dots in Fig. 2) becomes longer, i.e., a longer read-out time is required for a fixed sampling rate and decreased voxel dimension. For $\Delta x = 5 \text{ mm}$, 18% of the initial magnetization is lost for $t = TE = 24 \text{ msec}$; whereas 60% is lost at $TE = 40 \text{ msec}$ for $\Delta x = 3 \text{ mm}$. The attenuation is even worse for smaller voxels, because severe T_2^* -damping further contributes to signal attenuation as TE becomes greater than T_2^* . We note that for larger regions, such as the trachea or the large bronchi, where the ADC is closer to the free-air estimate, the attenuation is correspondingly worse (e.g., more than half of the magnetization would be lost at $t = TE$ for $\Delta x = 5 \text{ mm}$).

Thus for the human lung, the 5-mm linear voxel dimension, to which we were led above by consideration of the susceptibility-induced T_2^* and the desire to acquire an entire slice with a single rf excitation, is also appropriate for preserving the echo amplitude against decay due to diffusion. Further, a coarse grid (32×64 or 64×64) will improve imaging speed and greatly improve the number of images that can be acquired from a single bolus of HP gas with useful SNR as compared to the finer grids typically employed in ^3He lung MRI.

EXPERIMENTAL METHODS

^3He Polarization and Delivery

Samples of hyperpolarized ^3He are prepared through the spin-exchange optical pumping technique (34) in a dedi-

cated polarization apparatus. A 150-W diode-laser array (model CZ-150, Opto Power Corp., Tucson, AZ) is used to polarize ^3He in 45 ml valved Pyrex glass vessels. The vessels contain a mixture of 99% ^3He and 1% N_2 gas at 10 atm total pressure at 23°C, and a few hundred milligrams of distilled Rb metal. The vessels are filled using a separate gas-handling apparatus and may be refilled and reused indefinitely. Polarizations P of up to 40% have been achieved in these samples; 30% is typical for our imaging experiments.

The samples are transported ≈ 5 km to the MR scanner in a portable (≈ 40 G) set of Helmholtz coils. The polarization of each sample is determined before transport by comparing its NMR signal at 64.8 MHz to that of the protons in a glycerol sample. The polarization at the time the gas is delivered to the volunteer can then be calculated from the measured wall-relaxation time T_1 at 30 G for the vessels (≈ 35 hr for one and ≈ 15 hr for another). For the present experiment, we estimated $P \approx 28\%$.

The samples are delivered to the subject in a polyethylene bag, which is connected to ≈ 15 cm of tubing (16 mm i.d.) with a plastic tubing clamp attached. Just prior to imaging, the polarization vessel is removed from the portable coils and placed behind the scanner magnet, several feet from the bore opening along the field axis, where the fringe field of the actively shielded magnet is about 40 G. This location was selected because the field is reasonably strong (comparable to the field in which the vessel is polarized), yet the field gradients (~ 0.1 G/cm) are small enough to cause negligible T_1 relaxation of the gas (35). An all-plastic manifold consisting of stopcock valves and tubing is sealed (either by O-ring compression or barb fitting) to both a valve sidearm on the polarization vessel and the tubing connected to the plastic bag. The manifold has ports for a purge gas (pure N_2) and vacuum, so that the path between the vessel and the bag may be purged of room air prior to releasing the helium. About 1.5 L of pure N_2 gas is first admitted to the bag, then the vessel valve is opened. After the pressure in the vessel and the bag equilibrates (at 1 atm) the vessel valve is closed and the breathing tube is clamped shut. The gas bag is massaged for a few seconds to mix the gases thoroughly and then handed to the volunteer in the magnet.

^3He Imaging

All images were acquired with a 1.5 T Magnetom Vision whole-body imager (Siemens Medical Systems, Iselin, NJ). Based on the design shown by MacFall et al. (3), we constructed a 30-cm diameter pair of transmit-receive rf coils mounted onto posterboard. The coils were designed to have approximately the Helmholtz geometry for a typical human thorax and were tuned to the 48.5 MHz ^3He resonance at 1.5 T with a chest-loaded Q of about 10. The tuning and coupling of the coils were done on a typical subject outside of the magnet with fixed-value components. A proton-tuning box could be inserted into the coaxial line to retune the coils to the 63.6 MHz ^1H resonance.

Informed consent was obtained from all volunteers; the procedures were approved by the Washington University Internal Review Board. Five healthy subjects were imaged in the supine position with the coils placed anterior and posterior to the thorax and lightly strapped in place.

Breathing and imaging protocols varied somewhat among the subjects for these initial studies. The procedures were tolerated well in all cases. The following description applied specifically to the one subject for which data is presented. Coronal and axial proton images were acquired first to shim the applied field, to locate the lung position, and to choose three 10-mm-thick axial slices for rapid ^3He imaging. Slices were chosen 60 mm inferior to and 40 mm superior to a central slice. The slices were acquired in ascending order using an EPI sequence modified for a coarse pixel grid at the ^3He frequency. The scanner runs sinusoidal EPI read-out gradients with a read-out period of 600 μsec . Imaging parameters were: TR = 40.5 msec, TE = 12.1 msec, matrix 32×64 , FOV = 200×400 mm, 6.25×6.25 mm in-plane resolution. The echo-train length was 32, covering the entire slice with one excitation (flip angle $\approx 22^\circ$). Total time per image was thus the same as TR, and each set of three slices was acquired in 122 msec. The sequence uses a pre-pulse ($\approx 11^\circ$) for eddy-current correction. The three-slice set was acquired repetitively for 36.5 sec, starting just before the subject began inhaling polarized ^3He gas, for a total of 300 sets in 36.5 sec or one set every 0.12 sec.

Transmitter-output and receiver-gain settings were based on images of a large cylindrical ^3He Boltzmann-polarized phantom, images of a hyperpolarized vessel, and preliminary human studies. The Boltzmann phantom contains 13.8 standard liters of ^3He in a 6.4 L volume with an approximately equal amount of oxygen gas to reduce the ^3He T_1 to about 1 sec. When inserted into a tube-shaped loading vessel to simulate chest loading, a 150-mm axial slice can be imaged at thermal equilibrium using EPI with a typical single-shot SNR of 2. The loaded phantom was used to estimate the rf transmitter voltage corresponding to a 90° pulse for our chest coil. We have found this phantom useful for thoroughly testing coils and sequences, particularly since precious hyperpolarized gas is easily wasted if debugging is incomplete.

After hearing the ^3He imaging sequence commence, the volunteer released the tubing clamp and began breathing out of and back into the plastic bag. He was instructed to breath the entire volume contained in the bag, and his breathing period was 2.5–3.0 sec/cycle. He was able to rebreathe the ^3He - N_2 mixture in this fashion for the entire data-acquisition period.

RESULTS AND DISCUSSION

Two subsets of the 900 dynamic HP- ^3He lung images continuously acquired over 36.5 sec using the coarse-grid EPI technique are presented in Figs. 3 and 4. The images come from a healthy 27-year-old male volunteer. Each row in both figures corresponds to a three-slice set (upper, middle, lower) acquired in 0.12 sec. The five sets in Fig. 3 show the inflow of ^3He gas at 0.24-sec intervals as the ^3He - N_2 mixture was initially inhaled from the plastic bag. The five sets in Fig. 4 show the movement of gas at 0.72-sec intervals during one complete respiratory cycle; the top row was obtained at end-inspiration, about 10 sec after the subject started rebreathing. Since sets were acquired every 0.12 sec, one intervening set of images between each adjacent row is omitted in Fig. 3, and five

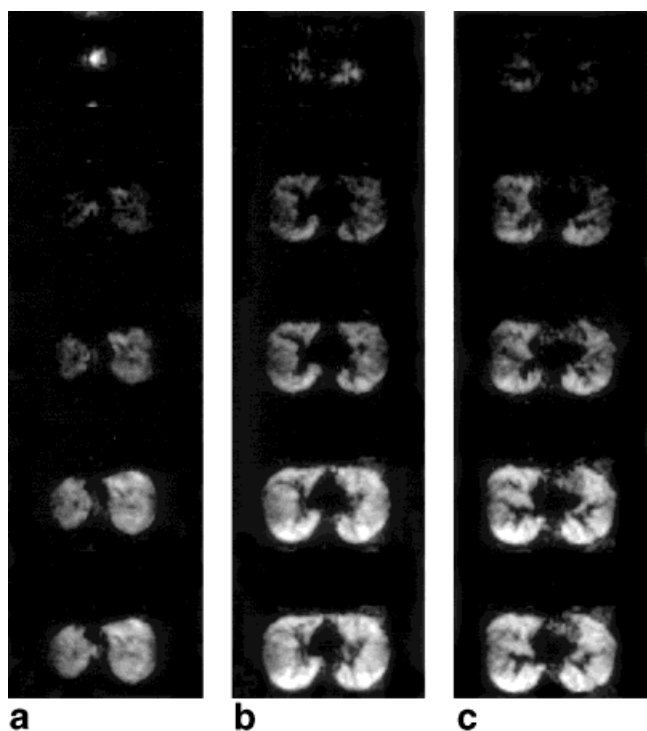


FIG. 3. A subset of ^3He MR images of ventilation in a healthy 27-year-old male volunteer using a coarse-grid EPI sequence. Moving in time from top to bottom, each row of images is the same three-slice set consisting of an upper (a), middle (b), and lower (c) axial slice (each 10-mm thick). A three slice set was acquired every 0.12 sec, although the temporal resolution displayed here between adjacent rows is 0.24 sec. These five sets correspond to the initial inspiration of HP ^3He . The average SNR at the first full inspiration (fifth row) is about 20. The field of view is 200×400 mm on a 32×64 matrix (in-plane voxel dimension 6.25×6.25 mm).

intervening sets are similarly omitted in Fig. 4. The intensity scales in Figs. 3 and 4 have not been individually normalized; the actual relative intensities are depicted.

The signal-to-noise ratio is about 20 at the first full inspiration and drops to about 6 after 24 sec of subsequent rebreathing (7–8 breathing cycles). To calculate the signal-intensity loss we would expect from rf excitation alone, we assume that each set of three slices excites the ^3He in 12% of the total lung volume (three out of a total of ≈ 25 axial slices for a typical lung), and that averaged over a breathing cycle, only half of the HP-gas is in the lung; the other half is in the bag. We also assume that averaged over many breathing cycles, the gas is thoroughly mixed and thus uniformly excited due to flowing in and out of the lungs. For a $22^\circ/11^\circ$ pulse/pre-pulse, we calculate a two-thirds decrease in magnetization after acquiring 200 three-slice sets in 24 sec. The calculated rf-excitation loss accounts for nearly all of the signal-intensity drop observed in the 24 sec after the first full inspiration, a somewhat surprising result considering that T_1 for ^3He in the lung is 30–40 sec (26). We thus might have expected to lose an additional 45–55% from T_1 relaxation. Possible explanations for the discrepancy include a much longer T_1 in the plastic bag (due to decreased wall-surface area), where the gas spends a portion of its time, and an overestimation of the tip angle,

which may have occurred if the subject loaded the coil differently than the loaded ^3He Boltzmann phantom.

Although small corrections are necessary, the raw images in Figs. 3 and 4 are not far from the goal of an accurate measurement of local ^3He concentration as a function of time for a single respiratory cycle—a true real-time picture of ventilation. For a single given respiratory cycle comprising about 20–25 three-slice sets, T_1 and rf excitation cause the observed global signal intensity to drop by only 10–12%. Based on Eq. [9] and the 6.25 mm linear voxel dimension, the signal attenuation at the center of k -space ($t = \text{TE} = 12.1$ msec) is 6% for $D = 0.25$ cm^2/sec in the alveoli, where diffusion is restricted. Small corrections could be made for these nonphysiological factors. We note that because of the axial slice geometry, the FOV in our images is only 200 mm in the phase-encoding direction, compared to 400 mm in the read-out direction. Thus, TE is about half of what it would be for the square FOV case presented in Fig. 2.

The images contain some artifacts, most notably the so-called “blooming” of the pulmonary vasculature, which was also observed to a lesser extent by Mugler et al. for segmented EPI echo-trains consisting of more than 3 echoes (17). The blood vessels, which contain no ^3He gas and should normally appear in relief, produce relatively large susceptibility gradients. The resulting short T_2^* and strong attenuation causes the vessels to appear (as dark areas of no signal) larger than their actual size. These

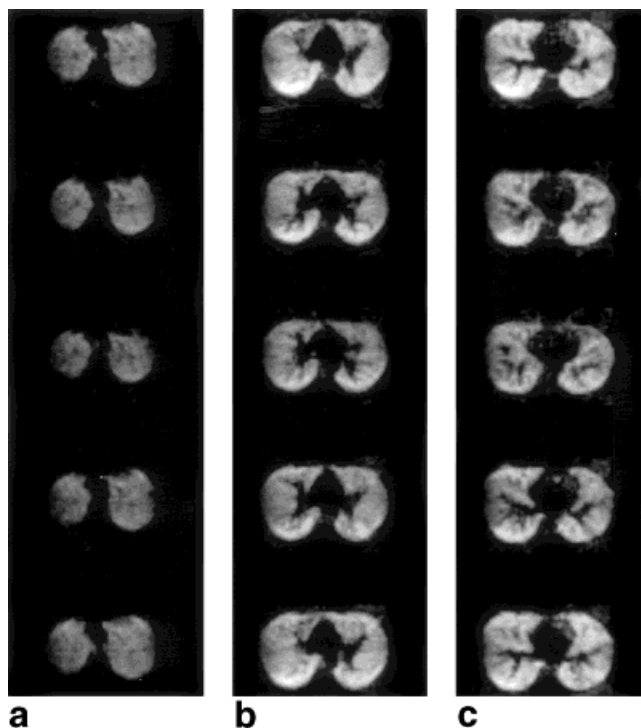


FIG. 4. A second subset of images from the same experiment as in Fig. 3 but displaying a full respiratory cycle. Time progresses from top to bottom, and each row consists of an upper (a), middle (b), and lower (c) 10-mm-thick axial slice. The temporal resolution between adjacent rows here is 0.72 sec (thus omitting five intervening sets of acquired images between each pair of adjacent rows). The five sets cover a single 3.0 sec respiratory cycle starting at end-inspiration (top row). Although this starting point occurred about 10 sec after the HP- ^3He was initially inspired, the average SNR is still about 15.

problems could be addressed with separate T_2^* maps of the lung (29) or complementary images of the vasculature (36). Perhaps a more suitable solution for HP gases would be to image at low applied magnetic fields (37). The HP magnetization and the SNR would be field-independent for the lossy human thorax in a broad range of fields (38,39). A 0.1 T field is not unreasonable and would yield a factor of 15 reduction in the bulk-susceptibility field inhomogeneities and a correspondingly reduced contribution to the transverse relaxation rate. There is also slight $N/2$ ghosting (40) in several of the images and some corresponding overlap with the primary image. Where visible, the ghosts have an intensity 3 or 4 times lower than the primary image. A larger FOV in the phase-encoding direction might be used where necessary to better separate the ghost at the expense of some temporal resolution.

There will necessarily be some motion of the lung through the imaging plane in this study, since images are acquired dynamically during breathing. Motion perpendicular to the axial slices will be more prominent near the moving diaphragm in healthy breathing. Motion in the plane of the slices is less of a problem, because the aim of this kind of imaging is to follow the gas, which does not necessarily follow the motions of the lung tissue or diaphragm.

Despite some signal attenuation and artifacts, changes in gas density due entirely to respiration are readily apparent in our images. While the signal intensity is not spatially homogeneous, the initial inspiration depicted in Fig. 3 shows that the gas does not appear to start in localized regions and spread out. Rather, all regions appear to start filling immediately, even on the 0.12 sec time scale. We also observe a higher ^3He gas concentration in the portions of the lung at the lowest gravitational potential (i.e., the posterior portion of our axial slices). Brookeman and co-workers have informed us that they also observe this dependent effect in their ^3He breath-hold experiments. The inhomogeneity is observed in the middle (Fig. 3b) and lower (Fig. 3c) slices in both image subsets. It develops immediately with the initial inspiration and is particularly prominent at end-inspiration. The single breathing cycle shown in Fig. 4 displays a remarkable periodicity, both of gas intensity and of structure in relief, as can be seen by comparing the top and bottom images in each column, both of which correspond to end-inspiration. This is better appreciated in ciné loops of the three slices. (These are available for viewing at <http://www.physics.wustl.edu/~saam/hemri.htm>.) The ciné loop of the upper slice shows, for example, the point of gas-flow reversal in the trachea (at end-inspiration and end-expiration) as a periodic signal blip; at times of greater flow through the trachea, the gas spreads on time scales short compared to TE laterally through the bronchial tree on inhalation or outside the rf coil towards the mouth on exhalation.

The voxel size in our images is significantly larger than what has been conventionally established in other HP gas work (typically 1–2 mm). We have effectively traded some spatial resolution for better temporal resolution and more efficient use of a single bolus of HP- ^3He gas. One important question is whether this trade-off is always necessary. Chen et al. (4), made use of a quasi-continuous supply of

HP- ^3He to the much smaller guinea pig lung (≈ 4 ml tidal volume) to visualize gas inflow with 0.2 mm in-plane resolution. Their effective temporal resolution of 0.1 sec was obtained by varying the delay of the acquisition window over several deliveries of a HP- ^3He bolus. A similar strategy for humans would require many times more HP- ^3He than is currently available or affordable for one human subject. The spiral-projection method employed by Ruppert et al. (14) has produced promising preliminary results in humans: dynamic images of a single thick (5-cm) section with about 4-mm linear in-plane voxel size. The spiral sequence makes efficient use of the available magnetization with good temporal resolution, although it relies on the acquisition of only a fraction ($1/16$) of the k -space plane to update the entire image every 15 msec. By comparison, our coarse-grid EPI technique updates the entire k -space plane with every image and is only about a factor of 2 slower in acquisition rate (though still much faster than the respiratory cycle).

The larger voxels may be acceptable for many applications. For example, the surgical target regions of interest in lung-volume reduction are much larger than the voxels in our study. In patients with emphysema, rapid coarse-grid EPI may be able to identify regions of air-trapping on exhalation, determine the temporal order of ventilation for more or less emphysematous tissue, and, in conjunction with a structural imaging modality such as computed tomography, identify regions of normal lung tissue that may be poorly ventilated because of surrounding emphysematous lung. More study is needed to determine the potential diagnostic utility of each of the methods proposed for dynamic HP-gas MRI.

CONCLUSIONS

We have addressed the issues of signal attenuation and magnetization consumption for the unique circumstance of a rapidly diffusing nonrenewable magnetization source. Through quantitative considerations and imaging of human volunteers, we conclude that rapid repetitive imaging of the lung gas space with a multiple echo sequence (EPI) and a single delivered bolus of hyperpolarized ^3He is indeed feasible using low flip angles, provided the voxels are not too small. We have developed and implemented a coarse-grid EPI pulse sequence for rapid HP- ^3He imaging of gas flow in the human lung. The images display some mild artifacts, but are of good quality and appear suitable for studying changes in gas density related to respiratory physiology. In the near future, we expect to image the entire lung in cross section with a temporal resolution of 1 sec or less. Further study of T_2^* inhomogeneity in the lung and/or application of the technique presented here at lower applied magnetic fields (~ 0.1 T) should significantly improve the image quality obtained with real-time dynamic HP- ^3He MRI.

ACKNOWLEDGMENTS

The authors thank Drs. J.J.H. Ackerman and V. Song for assistance in preliminary measurements. We thank Drs. S.S. Lefrak and R.M. Slone for helpful discussions, and Dr.

J.D. Cooper both for discussions and for additional financial support.

REFERENCES

- Mugler JP, Driehuys B, Brookeman JR, Cates GD, Berr SS, Bryant RG, Daniel TM, de Lange EE, Downs JH, Erickson CJ, Happer W, Hinton DP, Kassel NF, Maier T, Phillips CD, Saam BT, Sauer KL, Wagshul ME. MR imaging and spectroscopy using hyperpolarized ^{129}Xe gas: preliminary human results. *Magn Res Med* 1997;7:809–815.
- Kauczor H-U, Ebert M, Kreitner K-F, Nilgens H, Surkau R, Heil W, Hofmann D, Otten EW, Thelen M. Imaging of the lungs using ^3He MRI: preliminary clinical experience in 18 patients with and without lung disease. *J Magn Reson Imaging* 1997;7:538–543.
- MacFall JR, Charles HC, Black RD, Middleton H, Swartz J, Saam B, Driehuys B, Erickson C, Happer W, Cates GD, Johnson GA, Ravin CE. Human lung air spaces: potential for MR imaging with hyperpolarized ^3He . *Radiology* 1996;200:553–558.
- Chen XI, Chawla MS, Hedlund LW, Möller HE, MacFall JR, Johnson GA. MR microscopy of lung airways with hyperpolarized ^3He . *Magn Reson Med* 1998;39:79–84.
- Swanson SD, Rosen MS, Agranoff BW, Coulter KP, Welsh RC, Chupp TE. Brain MRI with laser-polarized ^{129}Xe . *Magn Reson Med* 1997;38:695–698.
- Cooper JD, Patterson GA. Lung volume reduction surgery for severe emphysema. *Semin Thorac Cardiovasc Surg* 1996;8:52–60.
- Brenner M, Yussen R, McKenna R Jr, Sciarba F, Gelb AF, Fischel R, Swain J, Chen JC, Kafie F, Lefrak SS. Lung volume reduction surgery for emphysema. *Chest* 1996;110:205–218.
- Haase A, Frahm J, Matthaei D, Hänicke W, Merboldt K-D. FLASH imaging: Rapid NMR imaging using low flip-angle pulses. *J Magn Res* 1986;67:258–266.
- Rinck PA, Petersen SB, Lauterbur PC. NMR imaging von fluorhaltigen substanzen. *Fortschr Röntgenstr* 1984;140:239–243.
- Kueth DO, Caprihan A, Fukushima E, Waggoner RA. Imaging lungs using inert fluorinated gases. *Magn Reson Med* 1998;39:85–88.
- Edelman RR, Hatabu H, Tadamura E, Li W, Prasad PV. Noninvasive assessment of regional ventilation in the human lung using oxygen enhanced magnetic resonance imaging. *Nature Med* 1996;2:1236–1239.
- West JB. *Pulmonary pathophysiology*, 4th edition. Baltimore: Williams and Wilkins; 1992. p 1–54.
- Mettler FA, Guiberteau MJ. *Essentials of nuclear medicine imaging*, 3rd edition. Philadelphia: Saunders; 1991. p 141–175.
- Ruppert K, Brookeman JR, Mugler JP. Real-time MR imaging of pulmonary gas-flow dynamics with hyperpolarized ^3He . In: *Proceedings of the International Society for Magnetic Resonance in Medicine*, 6th Scientific Meeting, Sydney, Australia, 1998. p 1909.
- Mansfield P. Multi-planar image formation using NMR spin echoes. *J Phys C* 1997;10:L55–58.
- Saam B, Yablonskiy DA, Conradi MS, Gierada DS. EPI imaging of lung function using hyperpolarized gas. In: *Proceedings of the International Society for Magnetic Resonance in Medicine* 6th Scientific Meeting, Sydney, Australia, 1998. p 1912.
- Mugler JP, Brookeman JR, Knight-Scott J, Maier T, de Lange EE, Bogorad PL. Interleaved echo-planar imaging of the lungs with hyperpolarized ^3He . In: *Proceedings of the International Society for Magnetic Resonance in Medicine* 6th Scientific Meeting, Sydney, Australia, 1998. p 448.
- Zhao L, Albert MS. Biomedical imaging using hyperpolarized noble gas MRI: pulse sequence considerations. *Nucl Instrum Meth A* 1998;402:454–460.
- Hennig J, Nauwerth A, Friedburg H. RARE imaging: a fast imaging method for clinical MR. *Magn Reson Med* 1986;3:823–833.
- Oshio K, Feinberg DA. GRASE (gradient- and spin-echo) imaging: a novel fast MRI technique. *Magn Reson Med* 1991;20:344–349.
- de Lange EE, Mugler JP, Brookeman JR, Knight-Scott J, Truweit JD, Teates CD, Daniel TM, Bogorad PL, Cates GD. Lung air spaces: MR imaging evaluation with hyperpolarized ^3He gas. *Radiology* 1999;210:851–857.
- Ebert M, Grossmann T, Heil W, Otten E, Surkau R, Leduc M, Bachert P, Knopp MV, Schad LR, Thelen M. Nuclear magnetic resonance imaging with hyperpolarised helium-3. *Lancet* 1996;347:1297–1299.
- Zhao L, Mulkern R, Tseng C-H, Williamson D, Patz S, Kraft R, Walsworth RL, Jolesz FA, Albert MS. Gradient-echo imaging considerations for hyperpolarized ^{129}Xe MR. *J Magn Reson B* 1996;113:179–183.
- Patyal BR, Gao J-H, Williams RF, Roby J, Saam B, Rockwell BA, Thomas RJ, Stolarski DJ, Fox PT. Longitudinal relaxation and diffusion measurements using magnetic resonance signals from laser-hyperpolarized ^{129}Xe nuclei. *J Magn Res* 1997;126:58–65.
- Yablonskiy DA. Quantitation of intrinsic magnetic susceptibility-related effects in a tissue matrix. Phantom study. *Magn Reson Med* 1998;39:417–428.
- Bachert P, Schad LR, Bock M, Knoop MV, Ebert M, Grossman T, Heil W, Hofmann D, Surkau R, Otten EW. Nuclear magnetic resonance imaging of airways in humans with use of hyperpolarized ^3He . *Magn Reson Med* 1996;36:192–196.
- Saam B, Happer W, Middleton H. Nuclear relaxation of ^3He in the presence of O_2 . *Phys Rev A* 1995;52:862–865.
- Kveder M, Zupancic I, Lahajnar G, Blinc R, Suput D, Ailion DC, Ganesan K, Goodrich C. Water proton NMR relaxation mechanisms in lung tissue. *Magn Res Med* 1988;7:432–441.
- Chen XI, Chawla MS, Cofer GP, Driehuys B, Hedlund LW, MacFall JR, Möller HE, Johnson GA. Spatially localized T_2^* measurements of hyperpolarized ^3He in the lung. In: *Proceedings of the International Society for Magnetic Resonance in Medicine* 6th Scientific Meeting, Sydney, Australia, 1998. p 450.
- Torrey HC. Bloch equations with diffusion terms. *Phys Rev* 1956;104:563–565.
- Karlicek RF, Lowe IJ. A modified pulsed gradient technique for measuring diffusion in the presence of large background gradients. *J Magn Reson* 1980;37:75–91.
- Slichter CP. *Principles of magnetic resonance*, 3rd edition. Berlin: Springer-Verlag; 1989. p 597–601.
- Mugler JP, Brookeman JR, Knight-Scott J, Maier T, de Lange EE, Bogorad PL. Regional measurement of the ^3He diffusion coefficient in the human lung. In: *Proceedings of the International Society for Magnetic Resonance in Medicine* 6th Scientific Meeting, Sydney, Australia, 1998. p 1906.
- Walker TG, Happer W. Spin-exchange optical pumping of noble-gas nuclei. *Rev Mod Phys* 1997;69:629–642.
- Cates GD, Schaefer SR, Happer W. Relaxation of spins due to field inhomogeneities in gaseous samples at low magnetic fields and low pressures. *Phys Rev A* 1988;37:2877–2885.
- Hatabu H, Gaa J, Kim D, Li W, Prasad PV, Edelman RR. Pulmonary perfusion: qualitative assessment with dynamic contrast-enhanced MRI using ultra-short TE and inversion recovery turbo FLASH. *Magn Reson Med* 1996;36:503–508.
- Darrasse L, Guillot G, Nacher PJ, Tastevin G. Low-field single shot ^3He MRI in human lungs. In: *Proceedings of the International Society for Magnetic Resonance in Medicine* 6th Scientific Meeting, Sydney, Australia, 1998. p 449.
- Black RD, Middleton HL, Cates GD, Cofer GP, Driehuys B, Happer W, Hedlund W, Johnson GA, Shattuck MD, Swartz JC. In-vivo ^3He MR images of guinea pig lungs. *Radiology* 1996;199:867–870.
- Edelstein WA, Glover GH, Hardy CJ, Redington RW. The intrinsic signal-to-noise ratio in NMR imaging. *Magn Reson Med* 1986;3:604–618.
- Hennel F. Multiple-shot echo-planar imaging. *Concepts Magn Reson* 1997;9:43–58.